Monthly Notices
of the
ROYAL ASTRONOMICAL SOCIETY

MNRAS **437,** 1259–1267 (2014)
Advance Access publication 2013 November 19

doi:10.1093/mnras/stt1948

Blocking low-eccentricity EMRIs: a statistical direct-summation *N*-body study of the Schwarzschild barrier

Patrick Brem,[1]⋆ Pau Amaro-Seoane[1] and Carlos F. Sopuerta[2]

[1]*Max Planck Institut für Gravitationsphysik (Albert-Einstein-Institut), D-14476 Potsdam, Germany*
[2]*Institut de Ciències de l'Espai (CSIC-IEEC), Facultat de Ciències, Campus UAB, Torre C5 parells, E-08193 Bellaterra, Spain*

Accepted 2013 October 9. Received 2013 October 9; in original form 2012 November 26

ABSTRACT

The capture of a compact object in a galactic nucleus by a massive black hole (MBH), an extreme-mass ratio inspiral (EMRI), is the best way to map space and time around it. Recent work on stellar dynamics has demonstrated that there seems to be a complot in phase space acting on *low-eccentricity* captures, since their rates decrease significantly by the presence of a blockade in the rate at which orbital angular momenta change takes place. This so-called 'Schwarzschild barrier' is a result of the impact of relativistic precession on to the stellar potential torques, and thus it affects the enhancement on lower eccentricity EMRIs that one would expect from resonant relaxation. We confirm and quantify the existence of this barrier using a large number of direct-summation *N*-body simulations with both a post-Newtonian and also, for the first time in a direct-summation code, a geodesic approximation for the relativistic orbits. The existence of the barrier prevents low-eccentricity EMRIs from approaching the central MBH via resonant relaxation. We confirm that the event rates for capture thus increase with the square of the distributed mass, in agreement with two-body relaxation. However, for nuclei with more than a few thousand $M_\odot$ in the inner 10 mpc, two-body relaxation is so efficient that compact objects do not decouple into gravitational wave-driven inspirals but are mostly driven into direct plunges, if the central MBH is not spinning. This leads to an apparent maximum event rate of about 1 Myr^{-1} for EMRIs originating from the inner 10 mpc.

Key words: stars: black holes – stars: kinematics and dynamics – galaxies: kinematics and dynamics – galaxies: nuclei.

1 INTRODUCTION

Massive black holes (MBHs), with masses ranging from some $10^4\,M_\odot$ to a few $10^9\,M_\odot$ are very likely present in the centre of most galaxies. Measurements of the kinematics of gas and stars in the central regions of nearby galaxies (see e.g. de Zeeuw 2001; Barth 2004; Kormendy 2004; Richstone 2004) have provided us with compelling evidence. Our own Milky Way is the galaxy for which we have the strongest observational proof of a central MBH. Data based on 16 yr of observations set the mass of the central super-massive black hole (SMBH) to $\sim 4 \times 10^6\,M_\odot$ (Eisenhauer et al. 2005; Ghez et al. 2005, 2008; Gillessen et al. 2009; Genzel, Eisenhauer & Gillessen 2010).

To interact with the central MBH, stars have to find themselves on 'loss-cone' orbits, which are orbits elongated enough to have a very close-in pericentre (Frank & Rees 1976; Lightman & Shapiro 1977; Hils & Bender 1995; Sigurdsson & Rees 1997; Amaro-Seoane & Spurzem 2001). While main-sequence stars are tidally disrupted when approaching the central MBH, compact objects [stellar black holes (BHs), neutron stars and white dwarfs] slowly spiral into the MBH via the gradual loss of energy in the form of gravitational radiation and are eventually swallowed after some $\sim 10^{3-5}$ orbits in the eLISA band (Amaro-Seoane et al. 2007, 2012a,b; Amaro-Seoane 2012). This is the best way to probe general relativity (Sopuerta 2010, 2013) and, thus, the factory of space and time around an MBH. We will also get additional information about the binary itself: in particular the masses of the system and the spins of the MBH can be measured to a level of precision without any precedent (see Amaro-Seoane et al. 2007, and references therein). Besides, the detection will provide us with information about the distribution of dark objects in galactic nuclei and globular clusters.

Producing extreme-mass ratio inspirals (EMRIs) is more difficult than producing tidal disruptions of stars (e.g. Rees 1988; Magorrian & Tremaine 1999; Syer & Ulmer 1999; Wang & Merritt 2004) because while disruptions require a single passage within a critical radius, an EMRI is a progressive phenomenon that is only successful if the small compact object suffers a large number of close encounters with the central MBH.

The requirement for an EMRI to be successful is not just to have a small periapsis, but that the gravitational radiation time-scale is sufficiently shorter than two-body relaxation, which could have a

⋆ E-mail: Patrick.Brem@aei.mpg.de

significant impact on the periapsis. Although the basic ideas are explained in detail in the recent review of Amaro-Seoane (2012), we deem it important to briefly summarize in the next paragraphs the fundamentals of the ideas of two different categories of EMRIs, since this will be crucial to understand the main results of this paper.

In a galactic nucleus without dissipation processes a star or BH suffers 'gravitational tugs' in the regime where the evolution is dominated by close encounters with other stars. These tugs, since they are driven by two-body relaxation, are *random* and caused by interacting with other stars that happen to have a very close position. The scattering rate is very similar in orbital energy E and angular momentum L. If the star gets close to a very low L, which is statistically probable, then the picture changes. The rate at which the star changes L will be much shorter than that at which it changes E. If we introduce a dissipation term in the picture, e.g. gravitational waves, the stellar BH follows the same initial evolution and, at some point, the compact object reaches the region in which it is on a very radial orbit. In this case, at every periapsis passage, the BH loses a significant amount of energy and, hence, the semimajor axis shrinks. If the process is efficient enough it becomes an EMRI. There are also other ways to bring compact objects on to close orbits around an MBH such as tidal breaking of binaries (Hills 1988; Yu & Tremaine 2003), which we do not consider here.

Stars and BHs in very radial orbits would then scatter faster in L than in E, so that they would end up as direct plunges, i.e. being swallowed by the MBH after an insignificant amount of gravitational wave bursts. Although their event rate is much larger, they do not allow us to get a full picture of the scenario as complete as compared with the slow inspiral of an EMRI (but see the recent work of Berry & Gair 2013, on bursting sources). The threshold lies around $\sim 10^{-2}$ pc (Hopman & Alexander 2005) and this is what has led up to now to the thought that the EMRI event rate should be dominated by the physical phenomena happening in the innermost volume around the MBH, of radius $\sim 10^{-2}$ pc.

However, while this is strictly true for Schwarzschild MBHs, the situation for spinning MBHs drastically changes the narrative. Recently, Amaro-Seoane, Sopuerta & Freitag (2013) proved that for Kerr MBHs, many of the configurations that would plunge in the Schwarzschild case do not plunge in the case of spinning central MBHs (especially for high spins), but spend a very large number of cycles in the eLISA band, i.e. they are simply high-eccentricity EMRIs. The authors prove that the event rate of both high-eccentric and also low-eccentric EMRIs is enhanced by the spin as compared to the Schwarzschild case by an amount that depends on the specific eccentricity and inclination of the orbit.

The fact that compact objects on a 'plunge' orbit have been envisaged as uninteresting has led to an effort to understand the phenomena that could lead to the creation of EMRIs in a volume of radius $\sim 10^{-2}$ pc. In this volume, resonant relaxation (RR) is very likely the most important process to lead compact objects to EMRI orbits (Rauch & Tremaine 1996; Hopman & Alexander 2006). Nonetheless, while in the absence of relativistic effects RR is expected to change the angular momentum of the stellar BHs very efficiently, Merritt et al. (2011, hereafter MAMW11) showed recently with a few direct N-body experiments that introducing relativistic precession effects are both a blessing and a curse for the inspiral event rate. Due to the fast Schwarzschild precession of the BH orbit, RR is quenched at high eccentricities, resulting in more inspirals than plunges. However, this quenching also means that, in total, fewer BHs will reach pericentres that are small enough to lead to an inspiral observable by gravitational wave detectors such as eLISA (Amaro-Seoane et al. 2012a,b; The eLISA Consortium 2013). In this paper, we present a statistical study of this Schwarzschild barrier (SB) with a set of thousands of direct-summation N-body simulations including relativistic corrections to study and quantify this effect. We implement the relativistic effects using a post-Newtonian (PN) formalism as in Kupi, Amaro-Seoane & Spurzem (2006) but also, and for the first time ever in a direct-summation integrator, a geodesic scheme.

This paper is organized as follows: In Section 2, we present the physical setup and the numerical methods used. In Section 3, we present general results for a fiducial setup while we explore a vast range of different stellar mass distributions in Section 4. We then discuss the SB in more detail in Section 5. The PN equations of motion and the solution of the geodesic equations used in this paper are given in Appendix A and B, respectively.

2 PHYSICAL SETTING AND NUMERICAL METHODS

Recently, MAMW11 estimated with a few direct-summation N-body simulations expanded with a statistical Monte Carlo study that the traditional EMRI event rate is markedly decreased by the presence of a blockade in the rate at which orbital angular momenta change takes place. This so-called SB is a result of the impact of relativistic precession on to the stellar potential torques. Although the authors find that some particles can penetrate the barrier, EMRIs are significantly suppressed in this scenario.

In analogy to MAMW11, the fiducial setup we consider consists of a central MBH of mass $M_\bullet$ surrounded by 50 stellar mass BHs of mass m_*. We fix the masses of the MBH and the stellar BHs at

$$M_\bullet = 10^6\,\mathrm{M}_\odot\,,$$
$$m_* = 50\,\mathrm{M}_\odot\,. \tag{1}$$

Initially, we distribute the BHs in phase space following a distribution of the form $N(a, e^2)\,\mathrm{d}a\,\mathrm{d}e^2 = N_0 \mathrm{d}a\,\mathrm{d}e^2$, with a the semimajor axis of the BHs and e their eccentricity. The semimajor axes range within $0.1 < a < 10\,\mathrm{Mpc}$.

This setup represents roughly a relaxed distribution of stellar mass objects around an MBH with mass density $\rho(r) \propto r^{-\gamma}$ with $\gamma = 2$ (Freitag, Amaro-Seoane & Kalogera 2006). We note that due to mass segregation (David, Durisen & Cohn 1987; Murphy, Cohn & Durisen 1991), the mass distribution of objects in the inner milliparsec of the Galactic nucleus is expected to be very top-heavy, making the choice of $m_* = 50\,\mathrm{M}_\odot$ not that unrealistic. However, in order to explore the physics of systems of other masses, we also consider systems of different N and m_*, but leave the distribution in a and e unchanged. This way we obtain an idea of how the event rates scale with the total distributed stellar mass in a small sphere around the SMBH.

We have to integrate the systems for a very long time with full PN corrections. Since we use a serial code at this point, the number of compact objects is limited due to numerical reasons to $N \approx 100$. On the other hand, for the region we consider here, a total mass of $2500\,\mathrm{M}_\odot$ already represents a realistic estimate of the distributed stellar mass within the inner 10 mpc of our Galaxy (Genzel et al. 2010).

2.1 Timescales

In order to have EMRI events, one needs BHs on orbits with pericentres of only a few gravitational radii ($r_\mathrm{g} = GM_\bullet/c^2$). This requires

the existence of physical mechanisms for driving BHs from their initial orbits on to very eccentric ones.

A purely Newtonian system has two different ways of exchanging angular momentum L (or eccentricity e) and orbital binding energy E (or semimajor axes a). The first one is by two-body scattering or non-resonant relaxation (NR) (see e.g. Spitzer 1987; Binney & Tremaine 2008; Amaro-Seoane 2012). Every time two objects come close they undergo scattering, changing the momenta of the scattering partners. This very basic mechanism exists in all gravitationally interacting systems from compact star clusters to galaxies. The associated time-scale for changing the angular momentum L of a given particle by $\Delta L \sim L$ is

$$\tau_{\rm NR} = 4.6\,{\rm Myr}\,\tilde{a}^{1/2}\left(\frac{M_\bullet}{10^6\,{\rm M}_\odot}\right)^{3/2}\left(\frac{m_*}{50\,{\rm M}_\odot}\right)^{-2}\left(\frac{N_{<1}}{5}\right)^{-1}, \quad (2)$$

where $N_{<1}$ is the number of stellar mass objects within a sphere of 1 Mpc and $\tilde{a}$ will denote the semimajor axis in mpc throughout the rest of the paper. The derivation of this equation, although trivial, can be found in MAMW11.

In Newtonian systems with a central massive object which dominates the gravitational potential, however, this relaxation mechanism is usually dominated by RR (Hopman & Alexander 2006).

The torque of a spherical distribution of stars of mass $M_*(r < a)$ inside a sphere of radius r on a BH with semimajor axis a leads to a retrograde orbital in-plane precession on a time-scale

$$\tau_{\rm M} = \frac{2\pi g(e)}{M_*(r<a)}\left(\frac{M_\bullet a^3}{G}\right)^{1/2}, \quad (3)$$

where the eccentricity-dependent function $g(e)$ is given by

$$g(e) = \frac{1+\sqrt{1-e^2}}{2\sqrt{1-e^2}}. \quad (4)$$

From equation (3) we can derive the time-scale of changes in the angular momentum, which for our system is given by

$$\tau_{\rm RR} \approx \frac{5.9\times10^4\,{\rm yr}}{\beta_s^2\,g(e)}\left(\frac{M_\bullet}{10^6\,{\rm M}_\odot}\right)^{1/2}\left(\frac{m_*}{50\,{\rm M}_\odot}\right)^{-1}\tilde{a}^{3/2}, \quad (5)$$

where β_s is a factor of order unity. For the derivation of equation (5), we defer the reader to reference MAMW11. This mechanism for relaxation, RR, is much more efficient than NR *at these distances* because the particles interact through coherent torques in resonant Keplerian orbits. It therefore could lead in principle to an enhancement in the EMRI event rate.

Relativistic effects introduce two new time-scales. The conservative Schwarzschild precession, appearing in particular at the first and second PN orders, causes a precession of the pericentre by an angle

$$\delta\Phi = \frac{3\pi G M_\bullet}{c^2}\frac{1}{a(1-e^2)} \quad (6)$$

per orbit. This leads to the following associated time-scale

$$\tau_{\rm SS} = \frac{\pi}{\delta\Phi}P(a) = \frac{2\pi c^2}{3(GM_\bullet)^{3/2}}a^{5/2}(1-e^2), \quad (7)$$

where $P(a) = 2\pi(a^3/GM_\bullet)^{1/2}$ is the orbital period. In a more convenient notation this yields

$$\tau_{\rm SS} \approx (2\times10^4\,{\rm yr})\,\tilde{a}^{5/2}(1-e^2)\left(\frac{M_\bullet}{10^6\,{\rm M}_\odot}\right)^{-3/2}. \quad (8)$$

The second important time-scale is the inspiral time $\tau_{\rm GR}$ via gravitational radiation only, which, for high eccentricities ($e \simeq 1$) is given by (Peters 1964)

$$\tau_{\rm GW} \approx \frac{5c^5}{256\,G^3}\frac{a^4}{m_* M_\bullet(m_*+M_\bullet)}(1-e^2)^{7/2} \quad (9)$$

$$\approx (1.16\times10^{13}\,{\rm yr})\,\tilde{a}^4(1-e^2)^{7/2} \times\left(\frac{m_*}{50\,{\rm M}_\odot}\right)^{-1}\left(\frac{M_\bullet}{10^6\,{\rm M}_\odot}\right)^{-2}, \quad (10)$$

for $M_\bullet \gg m_*$. This time-scale is highly sensitive to the eccentricity and semimajor axis and for a typical BH in the system much longer than any other relevant time. However, for particles very close to the central MBH, gravitational radiation may drive them gradually into the capture radius leading to an 'inspiral event'.

2.2 A direct-summation code with post-Newtonian and geodesic corrections

In order to integrate the initial configuration over time we use the publicly available PLANET code by Sverre Aarseth (Aarseth 1999, 2003), a direct summation N-body integrator. We have modified this code in order to introduce relativistic corrections to the Newtonian acceleration (Amaro-Seoane et al. 2012c). For the studies that we present here we have considered the following types of dynamics:

(i) purely Newtonian dynamics,
(ii) PN corrections,
(iii) relativistic geodesic equations for motion of the particles around the MBH.

In the purely Newtonian case, the integration is obviously done without modifications to the acceleration equations. In the second case, we add the PN corrections in the following way:

$$F = \overbrace{F_0}^{\rm Newt.} + \overbrace{\underbrace{c^{-2}F_2}_{\rm 1PN} + \underbrace{c^{-4}F_4}_{\rm 2PN}}^{\rm periapsis\ shift} + \overbrace{\underbrace{c^{-5}F_5}_{\rm 2.5PN}}^{\rm energy\ loss} + \overbrace{\mathcal{O}(c^{-6})}^{\rm neglected}, \quad (11)$$

where the individual F_i's denote the different PN corrections to the total force on a particle, which can be found in Appendix B.

Given the high mass ratios involved in EMRIs, their motion around an MBH can be also approximated by solving the geodesic equations of motion, neglecting in this way dissipative effects due to gravitational wave emission and higher order corrections in the mass ratio. In our case, the geodesic equations describe the exact trajectory of a test mass particle around a Schwarzschild MBH. Unlike the PN approximation, the geodesic equations are valid even in the last few $r_{\rm g}$ during a plunge or inspiral, however only in the limit $m_*/M_\bullet \to 0$. Some orbits are expected to migrate towards plunge or inspiral orbits at pericentre distances of $r_{\rm p} < 15r_{\rm g}$, where the errors of the PN approximation can already be quite significant (Yunes & Berti 2008). In order to test the existence of the SB at small distances, we have implemented these corrections in the PLANET code.

Since the geodesic equations do not contain dissipative terms, we compare the results of using them with the conservative PN implementations, i.e. setting the dissipative correction $F_5 = 0$ in equation (11).

At any given time all the active acceleration corrections are computed only between the MBH and a stellar BH object. The semimajor axis and eccentricity evolution is tracked by monitoring the

distances at periapsis $r_{\rm min}$ and apoapsis $r_{\rm max}$ using the standard relations

$$a = \frac{r_{\rm max} + r_{\rm min}}{2}\,, \tag{12}$$

$$e = \frac{r_{\rm max} - r_{\rm min}}{r_{\rm max} + r_{\rm min}}\,, \tag{13}$$

which are valid for any acceleration correction. This calculation does not require a PN expansion of the Keplerian expressions for a and e and is thus consistent with the purely Newtonian, PN and geodesic equations of motion.

We record a merger event whenever a particular has an instantaneous separation to the MBH of $r < 6\,r_{\rm g}$ (i.e. the Schwarzschild last stable orbit for circular orbits). We note that MAMW11 use $r < 8\,r_{\rm g}$ and thus might classify a few events that we call inspirals as plunges. We run $N_{\rm P} = 500$ simulations of the models described above, with different random seeds for the distribution of BHs, for a few Myr or until a merger event happens.

3 RESULTS FOR THE FIDUCIAL MODEL

For all the different sets P of simulations, we will compute the average time $\tau_{X,P}$ for the occurrence of a certain event X in the simulation set P in the following way:

$$\tau_{X,P} = \sum_{i=1}^{N_P} T_{i,P} \cdot \frac{1}{K_{X,P}}\,, \tag{14}$$

where the sum runs over all the total duration times $T_{i,P}$ of the N_P simulations and $K_{X,P}$ gives the total number of events X in the set P. Every simulation has been given a burn-in time of 10^4 yr, which is of the order of $\tau_{\rm RR} \approx 6 \times 10^4$ yr (see equation 5) in order to discard merger events due to particles being created extremely close to the MBH or even within the capture radius by the randomization routine.

In equation (14), the possible events X can be either e for an EMRI event or p for a plunge event. We define the error for our results as the Poisson error,

$$\sigma_{X,P} = \sqrt{K_{X,P}}\,. \tag{15}$$

The criterion for an event to be an inspiral event is taken to be

(i) $a_{\rm cap} < 1$ mpc and
(ii) $a_{\rm cap} < 1.5\,a(t_{\rm cap} - 500\,{\rm yr})$.

The second condition ensures that the semimajor axis of the merging body ($a_{\rm cap}$) has shrunk significantly prior to capture in order to dismiss plunges with low semimajor axis. The choice of 500 yr has empirically proven to distinguish perfectly between plunges and inspirals.

We summarize the event rates for our fiducial system in Table 1 and provide a more detailed analysis of the different simulation sets in this section.

3.1 Newtonian Simulations (Set SI)

Here, we present the results for our study using only purely Newtonian accelerations, i.e. only the term F_0 in equation (11). In this case, the individual objects exchange energy and angular momentum efficiently via RR. For the plunge time, using equation (14), we find

$$\tau_{\rm p,I} = (3.6 \pm 0.2) \times 10^4\,{\rm yr}\,. \tag{16}$$

Table 1. Comparison of the different event rates for the different scenarios studied.

Series	Plunge ($\rm yr^{-1}$)	Inspiral ($\rm yr^{-1}$)
SI: Newtonian	$(2.8 \pm 0.2) \times 10^{-5}$	–
SII: Only 2.5 PN	$(2.6 \pm 0.2) \times 10^{-5}$	$(4.3 \pm 0.6) \times 10^{-6}$
SIII: Full PN	$(5 \pm 1) \times 10^{-7}$	$(8 \pm 1) \times 10^{-7}$
SIV: 1PN, 2PN	$(1.3 \pm 0.2) \times 10^{-6}$	–
SV: Geodesics	$(1.3 \pm 0.3) \times 10^{-6}$	–

This agrees very well with the RR time-scale given by equation (5) for a typical particle, which confirms that this is the dominant mechanism at these radii for driving stellar objects into the central body in the purely Newtonian case. Of course, we do not identify any inspirals in the absence of gravitational radiation effects.

3.2 Simulations including 2.5 PN corrections (Set SII)

We now add only the dissipative effects due to gravitational radiation emission, which appear at 2.5 PN order, to the acceleration equations.

The analysis of the simulations now gives

$$\tau_{\rm p,II} = (3.8 \pm 0.2) \times 10^4\,{\rm yr}\,, \tag{17}$$

$$\tau_{\rm e,II} = (2.3 \pm 0.4) \times 10^5\,{\rm yr}\,. \tag{18}$$

Now, with the inclusion of the effects of gravitational radiation, gradual inspirals into the MBH are possible. This converts a subset of the plunge events from the simulations in set SI into inspiral events. However, the inspiral time $\tau_{\rm GW}$ given by equation (10) only becomes smaller than the RR time for

$$a(1-e) \lesssim 5\,r_{\rm g}\,, \tag{19}$$

which is smaller than the assumed capture radius. Thus, the efficient RR still drives the majority of particles into the capture radius before they can decouple from the stellar background and undergo a clean inspiral. In other words, the transfer of angular momentum to more eccentric orbits by RR is faster than the circularization by the dissipative 2.5 PN term.

3.3 Simulations including 1 PN, 2 PN and 2.5 PN corrections (Set SIII)

In this set of simulations, we include all PN terms up to 2.5 PN order in our calculations. This introduces prograde Schwarzschild precession in addition to the dissipation produced by gravitational-wave emission. This effect is expected to increase the associated times for inspiral and plunges, since it eliminates efficient RR at high eccentricities. We find

$$\tau_{\rm p,III} = (2.0 \pm 0.3) \times 10^6\,{\rm yr}\,, \tag{20}$$

$$\tau_{\rm e,III} = (1.3 \pm 0.2) \times 10^6\,{\rm yr}\,. \tag{21}$$

As expected, the inspiral and plunge times are now of the order of a two-body relaxation time, equation (2). We also see that the substantial difference between plunge and inspiral times seen in SII vanishes, because now the relaxation time-scale is much higher and gravitational radiation can more easily decouple the BH from the stellar background. Compared to the previous set, now the 2.5 PN

term is able to circularize and shrink the BH orbit faster than classical relaxation increases eccentricity.

3.4 Simulations including 1 PN and 2 PN corrections (Set SIV)

In order to compare our PN results with the results using geodesic equations of motion, we also ran a set of simulations with only the conservative 1 PN and 2 PN terms. In this set, we find a plunge time of

$$\tau_{\rm p,IV} = (7.7 \pm 1.0) \times 10^5 \,{\rm yr}\,. \tag{22}$$

This is consistent with the time we would obtain from SIII when combining plunge and inspiral events and shows again that the 2.5 PN term does not change the important mechanisms for angular momentum transfer.

3.5 Simulations considering geodesic motion around the MBH (Set SV)

In this set of simulations, we investigate the system using Newtonian forces to describe the gravitational interactions between the stellar BHs and to describe the interaction between the MBH and individual stellar BHs we use the exact solution of the motion of a test mass in a Schwarzschild metric (geodesic motion). This does intrinsically exclude dissipative effects and therefore, the results of this subsection should be compared to those from the set SIV. In the limit of $m_* \ll M_\bullet$, the geodesic equations (in harmonic coordinates) expanded up to 2 PN order and the conservative 2PN equations agree (see Appendix A), and hence they are consistent descriptions at this level of approximation.

In this set of simulations, we obtain

$$\tau_{\rm p,V} = (8.0 \pm 3.0) \times 10^5 \,{\rm yr}, \tag{23}$$

which is consistent with $\tau_{\rm p,\,IV}$. This agreement means that the motion very close to the MBH is not relevant for the relaxation processes that drive BHs into plunge orbits.

4 SCALING WITH m_* AND N

In order to verify the dependence of event rates on the underlying astrophysical setup, we carry out further simulations similar to SI, SIII and SV, with different BH masses and number density. The capture rate, which gives the number of BHs that are driven into low angular momentum capture orbits per unit time, is given by

$$\Gamma_{\rm RR}(a){\rm d}a \approx \frac{N(a){\rm d}a}{\ln(L_c/L_m)t_{\rm RR}}, \tag{24}$$

see MAMW11, where L_c corresponds to the circular orbital angular momentum at semimajor axis a and L_m the angular momentum at which capture occurs. This is valid when RR is the dominant mechanism driving orbits to high eccentricities. We assume that all systems are in an equilibrium state where $N(a)$ is time independent. Using equation (5), the total capture rate can thus be written as

$$\Gamma_{\rm RR} = \int_0^\infty \Gamma_{\rm RR}(a){\rm d}a = \Gamma_{0,\rm RR}\left(\frac{N_{<1}}{5}\right)\left(\frac{m_*}{50\,{\rm M}_\odot}\right), \tag{25}$$

where the integral over the distribution is absorbed into the fitting parameter $\Gamma_{0,\,\rm RR}$ which is here defined as the capture rate for an isotropic distribution with $N_{<1} = 5$ and $m_* = 50\,{\rm M}_\odot$. The proportionality to Nm_* comes from equation (5). We now change the product Nm_* and measure the capture rate $\Gamma = \tau^{-1}$ as described in Section 3. The results are shown in Fig. 1 as the black dots, with all

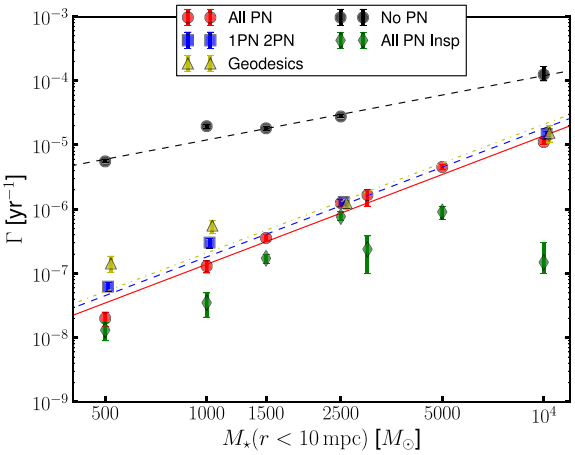

Figure 1. Total capture rates for different mass distributions. The black dots are models without GR precession and fitted to the dependence given by equation (25). Red, blue and yellow points are fitted to equation (26). The green diamonds give the pure inspiral rates. The specific mass models used are described in Table 2. Points belonging to the same mass model have been offset slightly along the horizontal axes to create less overlap.

Table 2. Stellar mass distributions used in this section.

M_* in $\rm M_\odot$	Individual m_* in $\rm M_\odot$	$N_{<10}$
500	10	50
1000	10	100
1500	10−50*	50
2500	50	50
3000	10−50*	100
5000	100	50
10 000	100	100

*Distributed according to a 'top-heavy', uniform distribution in mass, expected due to mass segregation (Bartko et al. 2010).

PN terms off. The black line is the best fit assuming the slope given by equation (25). The results agree very well with the assumption of RR being the dominant mechanism in the case of no GR precession. The best fit gives $\Gamma_{0,\,\rm RR,\,I} = (3.0 \pm 0.3) \times 10^{-5}\,{\rm yr}^{-1}$.

If we switch on GR precession and hence the SB, RR is quenched at high eccentricities and we expect non-resonant two-body relaxation to be dominant. In this case, $t_{\rm RR}$ has to be replaced by $t_{\rm NR}$ in equation (25) and the scaling becomes

$$\Gamma_{\rm NR} = \Gamma_{0,\rm NR}\left(\frac{N_{<1}}{5}\right)^2\left(\frac{m_*}{50\,{\rm M}_\odot}\right)^2, \tag{26}$$

where we have used equation (2). We show the capture rates for all PN terms, geodesic equations and only the precession terms 1PN and 2PN in Fig. 1. The mass distributions used are summarized in Table 2. The slope agrees very well with the dependence given by equation (26). Within a certain scatter and especially for larger total stellar masses, the rates for the PN and geodesic equations agree. We find $\Gamma_{0,\,\rm NR,\,III} = (8.7 \pm 1.0) \times 10^{-7}\,{\rm yr}^{-1}$ and $\Gamma_{0,\,\rm NR,\,IV} = (11.3 \pm 1.6) \times 10^{-7}\,{\rm yr}^{-1}$ for all PN and precession only PN terms, respectively. The geodesic equations give $\Gamma_{0,\,\rm NR,\,V} = (13.0 \pm 3.5) \times 10^{-7}\,{\rm yr}^{-1}$ and therefore agreement within 1σ.

Γ is the total capture rate, no matter whether a clean inspiral or a direct plunge, but the most interesting event rate for gravitational wave (GW) detectors is the inspiral rate. In Fig. 1, we also plot the pure inspiral rate for the run with all PN terms as green diamonds. For small background masses, two-body relaxation is slow and the inspiral rates are low as well. However, for high masses, two-body relaxation is so fast that the vast majority of events will be plunges, because decoupling into inspiral orbits occurs only for small semimajor axes. This results in an effective maximum event rate around 1 Myr^{-1}. Increasing the stellar mass further inhibits the formation of clean inspirals.

5 SCHWARZSCHILD BARRIER

In Fig. 1, we clearly see that for simulations with GR precession, the capture rates follow the scaling given by NR and not RR. This means that indeed RR is quenched at the low semimajor axes and high eccentricities relevant for capture. We want to show this barrier in energy-angular momentum space, using the results of our fiducial setup.

The 'SB' quenches RR for high eccentricities. This causes BHs to remain at a certain eccentricity value for a longer time. In order to visualize this, we construct a map in the $(a, 1-e)$ plane showing for each bin the percentage of BHs that remained in this bin for more than a time $\tau_{\rm cor} \approx t_{\rm RR}/10$. We show this value for the conservative PN simulation, series IV, in Fig. 2, where we subtracted the no PN values, series I.

If we consider our specific setup, there are three different regions in the $(a, 1-e)$ plane where different mechanisms are efficient. In the rightmost region, where pericentres are large, RR plays the dominant role. The left-hand border of this region is roughly given by the appearance of the Schwarzschild precession which inhibits the BHs from experiencing coherent torques. Following the derivation in MAMW11, the time-scale for changes in angular momentum due to an enclosed distribution of stars with mass m_* acting as a coherent torque is the RR time-scale, equation (5). The number of stars within a sphere delimited by the BHs semimajor axis, $N(a)$ is related

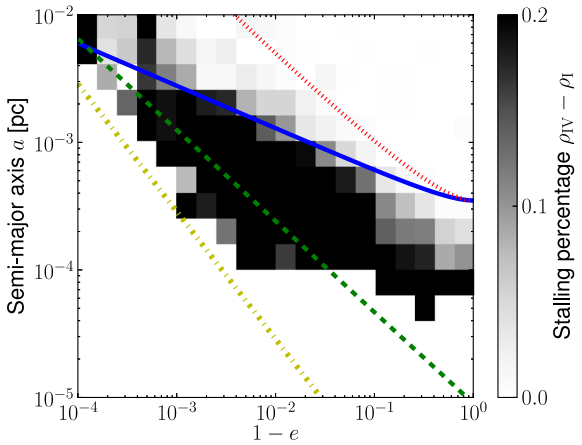

Figure 2. Percentage of BHs stalling in their respective bin for more than a time $t_{\rm RR}/10$ for the series IV simulation, where we subtracted the same values measured for the series I (no PN) simulation. The relative stalling becomes significantly higher left of the SB (*blue solid* line, equation (30)) as RR becomes inefficient. The *green dashed* line marks the decoupling into EMRI orbits from NR (equation (31)). The capture criterion $r < 8\,r_{\rm g}$ is marked by the *yellow dash–dotted* line. Left of the *red dotted* line, Schwarzschild precession becomes faster than mass precession.

to the density profile $\rho(r)$. For a general power law $\rho(r) \propto r^{-\gamma}$, the number of stars within a certain radius a becomes

$$N(r < a) = N_{<1}\tilde{a}^{3-\gamma}\,, \tag{27}$$

where $N_{<1}$ is the number of stars within a sphere of radius 1 mpc. The condition for the SB is that the relativistic precession time-scale, equation (7), becomes smaller than $\tau_{\rm RR}$, i.e.

$$a(1-e^2)^{1/2} = \frac{3\,G}{2\pi c^2}\frac{M_\bullet^2}{m_*}\sqrt{N(r<a)}\,. \tag{28}$$

In our model with $\gamma = 2$ and $N_{<1} \approx 5$, we obtain the relation

$$N(r < a) \approx 5\,\tilde{a}\,, \tag{29}$$

and thus the barrier at

$$\tilde{a}_{\rm SB} \approx C_{\rm SB}(1-e^2)^{-1/3}\,, \tag{30}$$

where $C_{\rm SB} \approx 0.35$ in this particular order of magnitude comparison. This line is shown in blue in Fig. 2. The bottom-left side of it is the region where RR is inefficient. This leads to a rising number of particles that stall in this area, indicated by black bins. The white area on the top-right side of the barrier marks where RR is unaffected as compared to the 'no PN' case. The area below $a = 10^{-4}$ pc is largely white because no particles where registered there.

We also show as the red dotted line the limit where $\tau_{\rm SS} = \tau_M$, equations (7) and (3). On the left of this line, GR precession is faster than mass precession and thus the assumption of τ_M being the shortest relevant coherence time breaks down. Starting from this line to the left, RR is already expected to become less and less efficient until it completely vanishes at the SB. From there on towards higher eccentricities, NR dominates the evolution.

If we also consider the dissipative PN term, the next delimiter is placed by the inspiral time-scale $\tau_{\rm GW}$. As soon as $\tau_{\rm GW} < \tau_{\rm NR}$, BHs decouple from the stellar background and inspiral gradually, driven by energy loss through gravitational radiation. The condition for this, using equation (10) and equation (2), yields

$$\tilde{a}_{\rm GW} \approx 1.5\times10^{-2}\left(\frac{M_\bullet}{10^6\,\mathrm{M}_\odot}\right)\left(\frac{m_*}{50\,\mathrm{M}_\odot}\right)^{-2/7} \times\left(\frac{N_{<1}}{5}\right)^{-2/7}(1-e^2)^{-5/7}\,. \tag{31}$$

This line for gravitational capture against NR is shown in green in Fig. 2. If BHs want to inspiral as EMRIs, they have to cross the black region until they reach the left of the green line. We defer the reader to MAMW11 for a more detailed presentation of the different delimiters for different number densities and masses.

6 DISCUSSION

Recently, MAMW11 estimated with a few direct-summation N-body simulations expanded with a statistical Monte Carlo study that the 'traditional EMRI' event rate is markedly decreased by the presence of a blockade in the rate at which orbital angular momenta change takes place. This so-called 'SB' is a result of the impact of relativistic precession on to the stellar potential torques. Although the authors find that some particles can penetrate the barrier, EMRIs are significantly suppressed in this scenario.

In this study, we investigated the effects of relativistic corrections on the event rates for EMRIs compared to Newtonian dynamics using a PN approach as presented in the original work of Kupi et al. (2006) but also and for the first time with the implementation of geodesic equations. For this purpose, we ran different sets of

≈500 simulations each, for combined durations of ∼100 Myr in order to obtain statistically solid results. We confirm the quenching of RR in the presence of Schwarzschild precession, i.e. the SB. Comparing full PN simulations (up to order 2.5) with the Newtonian ones, we find a ratio of the time-scales for the capture (combined plunge and inspiral) of

$$\tau_{\rm GR}/\tau_{\rm Newtonian} \approx 30 \pm 10 \quad (32)$$

and for the absolute value for our setup an EMRI event rate of $\lesssim 1\,{\rm Myr}^{-1}$.

In order to investigate the validity of the barrier at high eccentricities and very small pericentres, we have implemented the geodesic equations of motion around the MBH as an alternative to the PN corrections. We find that the results we obtain from both methods are consistent although the relativistic precession they predict is significantly different near the last stable orbit. This suggests that the stellar dynamics of the systems we have studied does not access significantly the regime where the dynamics as described by the geodesic equations and the PN corrections is different.

We have further verified the scaling of capture rates with the number of stellar mass objects and their mass. We show that in the case of Schwarzschild precession, the rates are determined by the NR time-scale, whereas in the non-precessing case we recover the capture rates given by RR. We see that for the pure EMRI event rates, an upper limit of $\Gamma \approx 1\,{\rm Myr}^{-1}$ appears for isothermal distributions and EMRIs originating within the inner 10 mpc. This is due to the inefficient relaxation mechanisms at low M_* and the too fast relaxation at high M_*. This maximum lies roughly in the mass range we expect for our own Galactic nucleus around our fiducial model at $M_* = 2500\,{\rm M}_\odot$ (Genzel et al. 2010).

We plan on expanding our scheme to use with general direct-summation *N*-body codes. This will allow us to investigate realistic galactic nuclei with a realistic number of stars and thus make more precise statements about the absolute event rates.

ACKNOWLEDGEMENTS

This work has been supported by the Transregio 7 'Gravitational Wave Astronomy' financed by the Deutsche Forschungsgemeinschaft DFG (German Research Foundation). The simulations were run on the ATLAS cluster of the Albert-Einstein-Institute Hannover. CFS acknowledges support from the Ramón y Cajal Programme of the Spanish Ministry of Education and Science, contract 2009-SGR-935 of AGAUR, and contracts FIS2008-06078-C03-03, AYA-2010-15709 and FIS2011-30145-C03-03 of MICCIN. We acknowledge the computational resources provided by the BSC-CNS (contracts AECT-2012-1-0008 and AECT-2012-2-0014) and CESGA (contracts CESGA-ICTS-221 and ICTS-CESGA-234).

REFERENCES

Aarseth S. J., 1999, PASP, 111, 1333
Aarseth S. J., 2003, Gravitational N-Body Simulations. Cambridge Univ. Press, Cambridge
Amaro-Seoane P., 2012, preprint (arXiv:1205.5240)
Amaro-Seoane P., Spurzem R., 2001, MNRAS, 327, 995
Amaro-Seoane P., Gair J. R., Freitag M., Miller M. C., Mandel I., Cutler C. J., Babak S., 2007, Class. Quantum Gravity, 24, 113
Amaro-Seoane P. et al., 2012a, Gravit. Waves Notes, 6, 4
Amaro-Seoane P. et al., 2012b, Class. Quantum Gravity, 29, 124016
Amaro-Seoane P., Brem P., Cuadra J., Armitage P. J., 2012c, ApJ, 744, L20
Amaro-Seoane P., Sopuerta C. F., Freitag M. D., 2013, MNRAS, 429, 3155
Barth A. J., 2004, in Ho L. C., ed., Coevolution of Black Holes and Galaxies. Cambridge Univ. Press, Cambridge, p. 21
Bartko H. et al., 2010, ApJ, 708, 834
Berry C. P. L., Gair J. R., 2013, MNRAS, 429, 589
Binney J., Tremaine S., 2008, in Binney J., Tremaine S., eds, Galactic Dynamics: Second Edition. Princeton Univ. Press, Princeton, NJ
Blanchet L., 2006, Living Rev. Relativ., 9, 4
David L. P., Durisen R. H., Cohn H. N., 1987, ApJ, 313, 556
de Zeeuw T., 2001, in Kaper L., van den Heuvel E. P. J., Woudt P. A., eds, ESO Astrophys. Symp., Black Holes in Binaries and Galactic Nuclei. Springer, Berlin, p. 78
Eisenhauer F. et al., 2005, ApJ, 628, 246
The eLISA Consortium, 2013, preprint (arXiv:1305.5720)
Frank J., Rees M. J., 1976, MNRAS, 176, 633
Freitag M., Amaro-Seoane P., Kalogera V., 2006, ApJ, 649, 91
Genzel R., Eisenhauer F., Gillessen S., 2010, Rev. Mod. Phys., 82, 3121
Ghez A. M., Salim S., Hornstein S. D., Tanner A., Lu J. R., Morris M., Becklin E. E., Duchêne G., 2005, ApJ, 620, 744
Ghez A. M. et al., 2008, ApJ, 689, 1044
Gillessen S., Eisenhauer F., Trippe S., Alexander T., Genzel R., Martins F., Ott T., 2009, ApJ, 692, 1075
Hills J. G., 1988, Nat, 331, 687
Hils D., Bender P. L., 1995, ApJ, 445, L7
Hopman C., Alexander T., 2005, ApJ, 629, 362
Hopman C., Alexander T., 2006, ApJ, 645, 1152
Kormendy J., 2004, in Ho L. C., ed., Coevolution of Black Holes and Galaxies. Cambridge Univ. Press, Cambridge, p. 1
Kupi G., Amaro-Seoane P., Spurzem R., 2006, MNRAS, L77
Lightman A. P., Shapiro S. L., 1977, ApJ, 211, 244
Magorrian J., Tremaine S., 1999, MNRAS, 309, 447
Merritt D., Alexander T., Mikkola S., Will C. M., 2011, Phys. Rev. D, 84, 044024 (MAMW11)
Misner C. W., Thorne K. S., Wheeler J. A., 1973, Gravitation. Freeman & Co., San Francisco
Murphy B. W., Cohn H. N., Durisen R. H., 1991, ApJ, 370, 60
Peters P. C., 1964, Phys. Rev., 136, 1224
Rauch K. P., Tremaine S., 1996, New Astron., 1, 149
Rees M. J., 1988, Nature, 333, 523
Richstone D., 2004, in Ho L. C., ed., Coevolution of Black Holes and Galaxies. Cambridge Univ. Press, Cambridge, p. 280
Sigurdsson S., Rees M. J., 1997, MNRAS, 284, 318
Sopuerta C. F., 2010, Gravit. Waves Notes, 4, 3
Sopuerta C. F., 2013, in Auger G., Binétruy P., Plagnol E., eds, ASP Conf. Ser. Vol. 467, 9th LISA Symposium. Astron. Soc. Pac., San Francisco, p. 69
Spitzer L., 1987, Dynamical Evolution of Globular Clusters. Princeton Univ. Press, Princeton, NJ, p. 191
Syer D., Ulmer A., 1999, MNRAS, 306, 35
Wang J., Merritt D., 2004, ApJ, 600, 149
Yu Q., Tremaine S., 2003, ApJ, 599, 1129
Yunes N., Berti E., 2008, Phys. Rev. D, 77, 124006

APPENDIX A: GEODESIC EQUATIONS FOR A PARTICLE ORBITING A BLACK HOLE

In this appendix, we write down the geodesic equations of motion in a form that is suitable to be included in an *N*-body code that uses a Newtonian-type formulation of the equations of motion. In order to compare results with the cases where PN corrections are used, we write the geodesic equations using harmonic coordinates for Schwarzschild, which are compatible with the harmonic gauge condition of PN theory.

Since our particles represent stellar objects, we need to consider the geodesics for massive particles (i.e. time-like geodesics). Given our system of spacetime coordinates $\{x^\mu\} = \{t, x^i\}$ ($\mu, \nu, \ldots = 0{-}3$; $i, j, \ldots = 1{-}3$), a geodesic will be given by $\{x^\mu(\tau)\}$, where

τ denotes the particle's proper time. The components of the velocity vector are defined as

$$u^\mu = \frac{\mathrm{d}x^\mu(\tau)}{\mathrm{d}\tau}\,. \tag{A1}$$

This four-velocity vector satisfies

$$g_{\mu\nu}u^\mu u^\nu = -c^2\,, \tag{A2}$$

where $g_{\mu\nu}$ is the Schwarzschild metric in our coordinate system and c denotes the speed of light. Since we are interested in geodesics, the velocity vector must satisfy the following equation of motion (Misner, Thorne & Wheeler 1973).

$$u^\nu \nabla_\nu u^\mu = 0\,, \tag{A3}$$

where ∇_μ denotes the canonical covariant derivative associated with the spacetime metric $g_{\mu\nu}$. Expanding this equation we have

$$\frac{\mathrm{d}u^\rho}{\mathrm{d}\tau} + \Gamma^\rho_{\mu\nu}u^\mu u^\nu = 0\,, \tag{A4}$$

being $\Gamma^\rho_{\mu\nu}$ the Christoffel symbols associated with the spacetime metric $g_{\mu\nu}$. They are given in terms of the metric by

$$\Gamma^\mu_{\alpha\beta} = \frac{1}{2}g^{\mu\nu}\left(\frac{\partial g_{\alpha\nu}}{\partial x^\beta} + \frac{\partial g_{\beta\nu}}{\partial x^\alpha} - \frac{\partial g_{\alpha\beta}}{\partial x^\rho}\right). \tag{A5}$$

Using the splitting of time and space, we can write the velocity vector as follows:

$$\boldsymbol{u} = u^t\frac{\partial}{\partial t} + u^i\frac{\partial}{\partial x^i}\,, \tag{A6}$$

where $\{u^t, u^i\}$ are the velocity components in the $\{t, x^i\}$ coordinate system:

$$u^t = \frac{\partial t(\tau)}{\partial\tau}\,, \quad u^i = \frac{\partial x^i(\tau)}{\partial\tau}\,. \tag{A7}$$

Therefore, on the trajectory of the particle we can write

$$u^i = \frac{\mathrm{d}x^i(t)}{\mathrm{d}t}\frac{\partial t}{\partial\tau} = v^i u^t \equiv \Gamma v^i\,, \tag{A8}$$

where v^i are the spatial components of the velocity

$$v^i = \frac{\mathrm{d}x^i(t)}{\mathrm{d}t} \tag{A9}$$

and Γ is the general relativistic version of the special relativistic gamma factor, which is given in terms of the components of the spatial velocity and the metric tensor as

$$\Gamma^2 = -\frac{c^2}{g_{tt} + 2g_{ti}v^i + g_{ij}v^i v^j}\,, \tag{A10}$$

which, in the weak-field limit ($g_{tt} \approx -c^2$, $g_{ti} \approx 0$, $g_{ij} \approx \delta_{ij}$), has the usual expression:

$$\Gamma^2 \approx \frac{1}{1-\frac{v^2}{c^2}}\,, \qquad \left(v^2 \equiv \delta_{ij}v^i v^j\right)\,. \tag{A11}$$

At this point, we can now adopt a Newtonian point of view by looking at the geodesic equations for the six quantities: $\{x^i(t), v^i(t)\}$, that is, for the spatial coordinates and spatial velocity components. They can be written as

$$\frac{\mathrm{d}x^i}{\mathrm{d}t} = v^i\,, \tag{A12}$$

$$\frac{\mathrm{d}v^i}{\mathrm{d}t} = f^i_{\mathrm{g}}\,, \tag{A13}$$

where the *forces*, f^i_{g}, are actually forces per unit mass, i.e. accelerations, since they should not depend on the mass of the body (according to the equivalence principle). Moreover, these specific forces depend on the spacetime metric (and its first derivatives) and on v^i. They can be written as

$$f^i_{\mathrm{g}} = v^i\,\Gamma^t_{tt} - \Gamma^i_{tt} + 2\left(v^i\,\Gamma^t_{tj} - \Gamma^i_{tj}\right)v^j + \left(v^i\,\Gamma^t_{jk} - \Gamma^i_{jk}\right)v^j v^k\,. \tag{A14}$$

Given initial conditions $\{x^i_o, v^i_o\}$ equations (A12, A13) have a unique solution $\{x^i(t), v^i(t)\}$. Note that the c^2 factor dividing the forces, when going to the right-hand side of the equation (multiplying the Christoffel symbols) will cancel the c^2 factor in the denominator of r_{g} [see expressions in equations (A22)–(A27)].

Since up to now the development has been quite general, let us now consider the case of a non-spinning (Schwarzschild) MBH of mass $M_\bullet$. The metric components, in harmonic coordinates, can be written in the following form:

$$g_{tt} = -\frac{1-\frac{r_{\mathrm{g}}}{r}}{1+\frac{r_{\mathrm{g}}}{r}}\,c^2, \tag{A15}$$

$$g_{ti} = 0\,, \tag{A16}$$

$$g_{ij} = \frac{1+\frac{r_{\mathrm{g}}}{r}}{1-\frac{r_{\mathrm{g}}}{r}}\,n_i n_j + \left(1+\frac{r_{\mathrm{g}}}{r}\right)^2\left(\delta_{ij} - n_i n_j\right), \tag{A17}$$

where

$$r = \sqrt{\delta_{ij}\,x^i x^j}\,, \qquad n^i = \frac{x^i}{r}\,, \qquad r_{\mathrm{g}} = \frac{GM_\bullet}{c^2}\,. \tag{A18}$$

From here, the components of the inverse metric are

$$g^{tt} = -\frac{1+\frac{r_{\mathrm{g}}}{r}}{1-\frac{r_{\mathrm{g}}}{r}}\,\frac{1}{c^2}\,, \tag{A19}$$

$$g^{ti} = 0\,, \tag{A20}$$

$$g^{ij} = \frac{1-\frac{r_{\mathrm{g}}}{r}}{1+\frac{r_{\mathrm{g}}}{r}}\,n^i n^j + \frac{1}{\left(1+\frac{r_{\mathrm{g}}}{r}\right)^2}\left(\delta^{ij} - n^i n^j\right), \tag{A21}$$

where $x_i = \delta_{ij}\,x^j$ and $n_i = \delta_{ij}\,n^j$.

The important thing to determine the forces is the computation of the Christoffel symbols. From their definition (A5), we find the following result

$$\Gamma^t_{tt} = 0\,, \tag{A22}$$

$$\Gamma^t_{ti} = \frac{r_{\mathrm{g}}}{r^2}\,\frac{n_i}{1-\left(\frac{r_{\mathrm{g}}}{r}\right)^2}\,, \tag{A23}$$

$$\Gamma^t_{ij} = 0\,, \tag{A24}$$

$$\Gamma^i_{tt} = \frac{r_{\mathrm{g}}}{r^2}\,\frac{1-\frac{r_{\mathrm{g}}}{r}}{\left(1+\frac{r_{\mathrm{g}}}{r}\right)^3}\,n^i\,c^2\,, \tag{A25}$$

$$\Gamma^i_{tj} = 0\,, \tag{A26}$$

$$\Gamma^i_{jk} = \frac{r_{\mathrm{g}}}{r^2}\,\frac{1}{1+\frac{r_{\mathrm{g}}}{r}}\left[\left(1+\frac{r_{\mathrm{g}}}{r}\right)n^i\left(\delta_{jk} - n_j n_k\right) - \frac{n^i n_j n_k}{1-\frac{r_{\mathrm{g}}}{r}} - 2n_{(j}\left(\delta^i_{k)} - n^i n_{k)}\right)\right]. \tag{A27}$$

And this determines completely the geodesic equations of motion in equations (A12) and (A13).

Finally, we can make a PN expansion of the equations of motion. That is, an expansion for $r_g/r \ll 1$ and $v/c \ll 1$. In our case, the expression for the *force* simplifies to (see equation A14 and equations A22–A27]

$$f_g^i = -\Gamma^i_{tt} + 2\,v^i\,\Gamma^t_{tj}v^j - \Gamma^i_{jk}v^j v^k\,. \tag{A28}$$

Expanding this we obtain

$$\begin{aligned} f_g^i = &-\frac{r_g c^2}{r^2}\left[1 - 4\frac{r_g}{r} + 9\left(\frac{r_g}{r}\right)^2 - 16\left(\frac{r_g}{r}\right)^3\right] n^i \\ &+2\,\frac{r_g c^2}{r^2}\left[1 + \left(\frac{r_g}{r}\right)^2\right]\left(\frac{n_j v^j}{c}\right)\frac{v^i}{c} \\ &-\frac{r_g c^2}{r^2}\left\{ n^i\left(\delta_{jk} - n_j n_k\right) - \left[1 + \left(\frac{r_g}{r}\right)^2\right] n^i n_j n_k \right. \\ &\left. -2\left[1 - \frac{r_g}{r} + \left(\frac{r_g}{r}\right)^2 - \left(\frac{r_g}{r}\right)^3\right] n_{(j}\left(\delta^i_{k)} - n^i n_{k)}\right)\right\} \\ &\times\frac{v^j}{c}\frac{v^k}{c}\,, \end{aligned} \tag{A29}$$

where the first two rows correspond to the first two terms in equation (A28). We have expanded in Taylor series the functions of r_g/r up to order $(r_g/r)^4$. We can now collect the terms and we find the following expression, which is valid to order 2 PN (see equation B1 below):

$$\begin{aligned} f_g^i = &-\frac{GM_\bullet}{r^2}n^i + \frac{GM_\bullet}{r^2}\left\{\left(\mathcal{A}_{1PN} + \mathcal{A}_{2PN}\right) n^i \right. \\ &\left. +\frac{\boldsymbol{n}\cdot\boldsymbol{v}}{c}\left(\mathcal{B}_{1PN} + \mathcal{B}_{2PN}\right)\frac{v^i}{c}\right\}, \end{aligned} \tag{A30}$$

where

$$\begin{aligned} &\frac{\boldsymbol{n}\cdot\boldsymbol{v}}{c} = \frac{\boldsymbol{x}}{cr}\frac{\mathrm{d}\boldsymbol{x}}{\mathrm{d}t} = \frac{1}{2cr}\frac{\mathrm{d}\boldsymbol{x}^2}{\mathrm{d}t} = \frac{1}{2cr}\frac{\mathrm{d}r}{\mathrm{d}t} = \frac{\dot r}{c}\,, \\ &v^2 = \boldsymbol{v}\cdot\boldsymbol{v} = \delta_{ij}v^i v^j \end{aligned} \tag{A31}$$

and

$$\mathcal{A}_{1PN} = 4\frac{r_g}{r} - \frac{v^2}{c^2}\,, \tag{A32}$$

$$\mathcal{A}_{2PN} = -9\left(\frac{r_g}{r}\right)^2 + 2\left(\frac{\boldsymbol{n}\cdot\boldsymbol{v}}{c}\right)^2\frac{r_g}{r}\,, \tag{A33}$$

$$\mathcal{B}_{1PN} = 4\,, \tag{A34}$$

$$\mathcal{B}_{2PN} = -2\frac{r_g}{r}\,. \tag{A35}$$

APPENDIX B: PN CORRECTIONS

The PN equations of motion used in our simulations can be written in the form given in equation (11). We can organize the different terms in the following form (which is similar to the one used above in equation A30 for geodesic equations):

$$\begin{aligned} f_g^i = &-\frac{GM}{r^2}n^i + \frac{GM}{r^2}\left\{\left(\mathcal{A}'_{1PN} + \mathcal{A}'_{2PN}\right) n^i \right. \\ &+\frac{\boldsymbol{n}\cdot\boldsymbol{v}}{c}\left(\mathcal{B}'_{1PN} + \mathcal{B}'_{2PN}\right)\frac{v^i}{c} \\ &\left. +\frac{\boldsymbol{n}\cdot\boldsymbol{v}}{c}\mathcal{A}'_{2.5PN}\,n^i + \mathcal{B}'_{2.5PN}\frac{v^i}{c}\right\}, \end{aligned} \tag{B1}$$

where here $M = m_* + M_\bullet$ is the two-body (MBH+BH) total mass. We list here the PN coefficients (see, e.g. Blanchet 2006, equation 131) for $m_* \neq 0$:

$$\mathcal{A}'_{1PN} = \frac{3}{2}\nu\left(\frac{\boldsymbol{n}\cdot\boldsymbol{v}}{c}\right)^2 - (1+3\nu)\frac{v^2}{c^2} + (4+2\nu)\frac{R_g}{r}\,, \tag{B2}$$

$$\begin{aligned} \mathcal{A}'_{2PN} = &-\frac{15}{8}\nu\,(1+3\nu)\left(\frac{\boldsymbol{n}\cdot\boldsymbol{v}}{c}\right)^4 \\ &+\nu\,(3-4\nu)\left[\frac{3}{2}\left(\frac{\boldsymbol{n}\cdot\boldsymbol{v}}{c}\right)^2 - \frac{v^2}{c^2}\right]\frac{v^2}{c^2} \\ &+\frac{R_g}{r}\left\{2\left(1 + \frac{25}{2}\nu + \nu^2\right)\left(\frac{\boldsymbol{n}\cdot\boldsymbol{v}}{c}\right)^2 \right. \\ &\left. +\nu\left(\frac{13}{2} - 2\nu\right)\frac{v^2}{c^2}\right\} - \left(9 + \frac{87}{4}\nu\right)\frac{R_g^2}{r^2}\,, \end{aligned} \tag{B3}$$

$$\mathcal{A}'_{2.5PN} = \frac{24}{5}\frac{R_g}{r}\frac{v^2}{c^2} + \frac{136}{15}\nu\left(\frac{R_g}{r}\right)^2\,, \tag{B4}$$

$$\mathcal{B}'_{1PN} = 4 - 2\nu\,, \tag{B5}$$

$$\begin{aligned} \mathcal{B}'_{2PN} = &-\frac{3}{2}\nu\,(3+2\nu)\left(\frac{\boldsymbol{n}\cdot\boldsymbol{v}}{c}\right)^2 + \nu\left(\frac{15}{2} + 2\nu\right)\frac{v^2}{c^2} \\ &-\left(2 + \frac{41\nu}{2} + 4\nu^2\right)\frac{R_g}{r}\,, \end{aligned} \tag{B6}$$

$$\mathcal{B}'_{2.5PN} = -\frac{24}{5}\nu\left(\frac{R_g}{r}\right)^2 - \frac{8}{5}\nu\frac{R_g}{r}\frac{v^2}{c^2}\,, \tag{B7}$$

where ν is the symmetric mass ratio, $\nu = m_* M_\bullet/M^2$, and $R_g = GM/c^2$. One can verify that the coefficients in equation (A32) to equation (A35) agree with equation (B2) to (B7) for $\nu = 0$.

This paper has been typeset from a TEX/LATEX file prepared by the author.